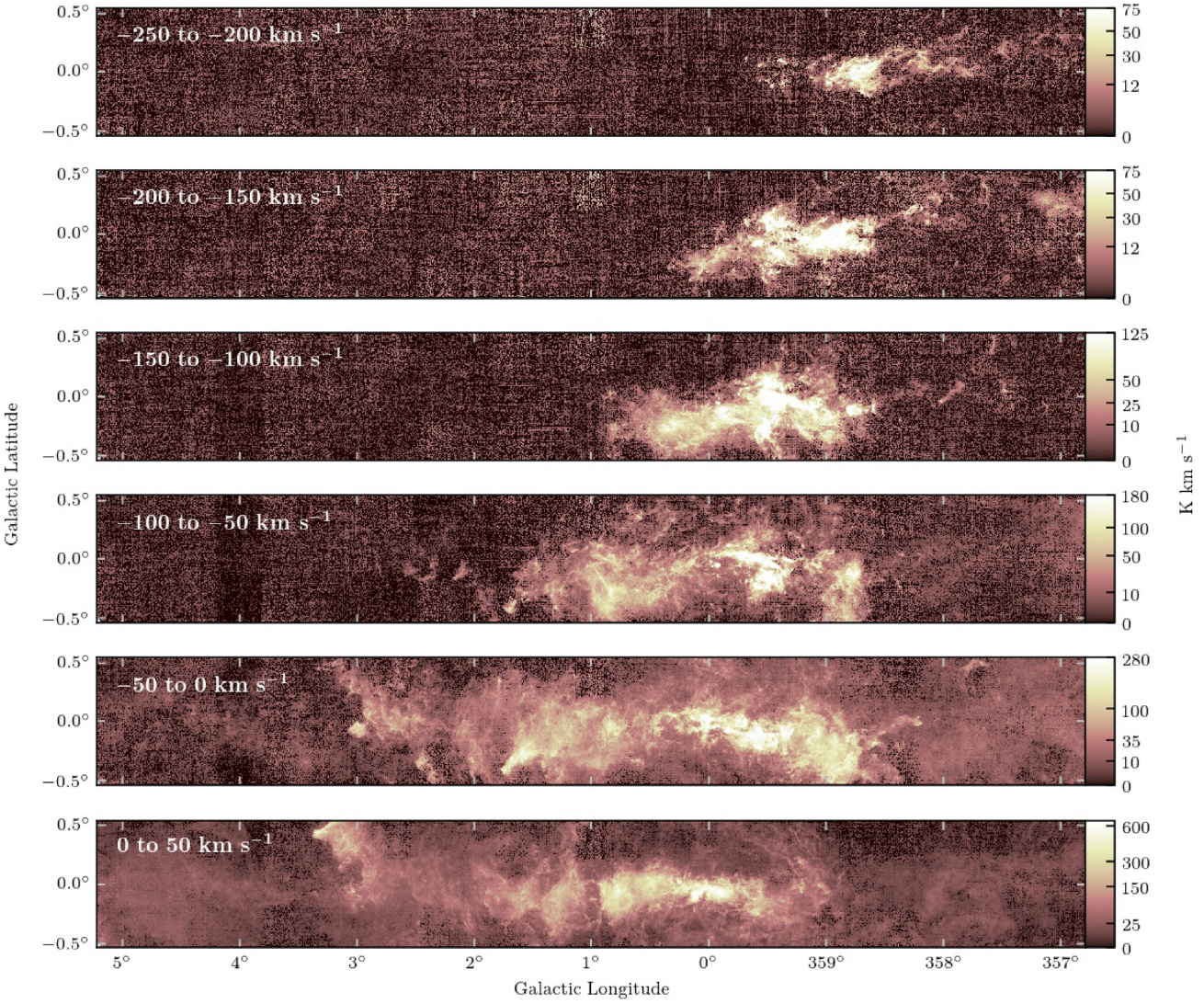

Figure 6. The integrated emission of the map, split into 50-km s^{-1} channels. The top map is −250 to −200 km s^{-1}; the second map is −200 to −150 km s^{-1}; the third map is −150 to −100 km s^{-1}; the fourth map is −100 to −50 km s^{-1}; the fifth map is −50 to 0 km s^{-1}; and the bottom map is 0 to 50 km s^{-1}.

of the latter that can be picked out in Fig. 8, including *The Brick* ($\ell \simeq 0.^{\circ}25$), the clouds of the dust ridge at $\ell = 0.^{\circ}3$–$0.^{\circ}5$, Sgr B2 at $\ell \simeq 0.^{\circ}7$, the 50- and 20-km s^{-1} clouds at $\ell = 359.^{\circ}9$–$360.^{\circ}0$, Sgr C at $\ell \simeq 359.^{\circ}4$, as well as the southern part of the loop structure discussed by Molinari et al. (2011b), Henshaw et al. (2016), and others, in terms of clouds orbiting the central potential. The known objects from Table 4 that were not detected by CUTEX, are plotted in Fig. 8 as white circles. In addition to these two sets of objects, there are at least as many that can be picked out by eye. This simple analysis thus has considerable potential as a discovery channel for finding previously unknown dense, compact sources in such data and will be investigated further in future work. Here, we briefly investigate whether or not such sources tend to be colder than their surroundings.

The source extraction with CUTEX was repeated on the data in Fig. 8 but, rather than the reciprocal map above, now the maxima were detected. The positions of both CUTEX samples were used to extract temperature and column densities from the results of Marsh et al. (2017), produced by the PPMAP procedure outlined in Marsh, Whitworth & Lomax (2015). The left-hand panel of Fig. 9 shows the total column density contained within the sources at each temperature within the PPMAP grid. There are 12 temperatures, evenly separated in log space between 8 and 50 K. The peak total column density is found at 18.4 K for the minima, compared with 21.7 K for the maxima. The positions of the same sources were used to extract values from the column-density-weighted mean temperature maps produced by PPMAP, and the cumulative distributions of these values are shown in the right-hand panel of Fig. 9.

The distribution of temperatures at the positions of the ^{12}CO/500-μm minima in Fig. 8 is weighted to lower values than that of the maxima. The former are therefore tracing denser, colder structures, probably with high optical depths in ^{12}CO and perhaps some degree of freeze-out of CO molecules on to dust grains. The minima generally form quite compact features that pick out many of the dense clouds studied by, e.g. Walker et al. (2018). By induction, high values, which tend to be extended, should therefore correspond to warmer areas of low ^{12}CO optical depth.

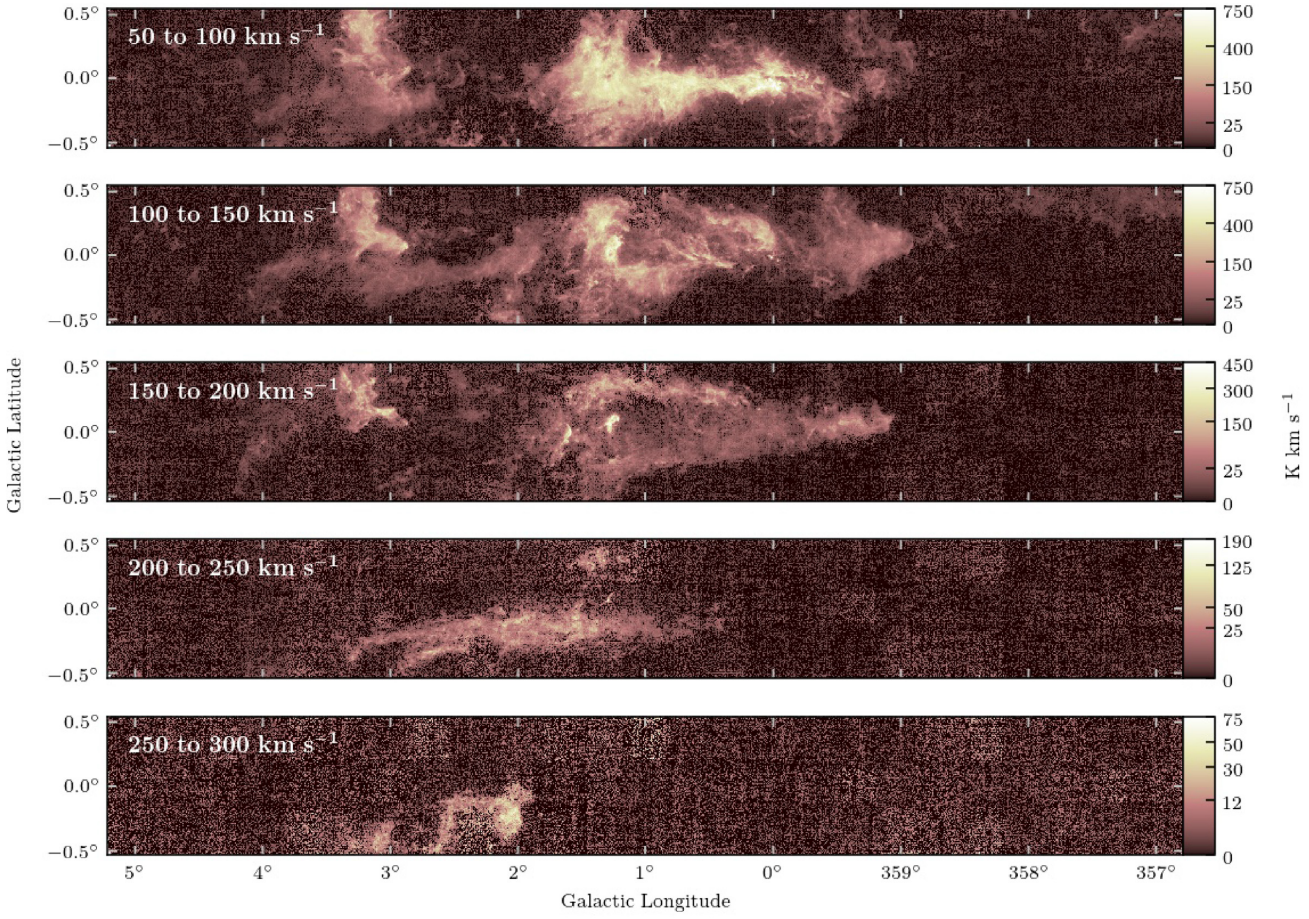

Figure 7. The integrated emission of ^{12}CO $J = 3 \rightarrow 2$, split into 50-km s^{-1} channels. From top to bottom, these are 50–100 km s^{-1}; 100–150 km s^{-1}; 150–200 km s^{-1}; 200–250 km s^{-1}; and 250–300 km s^{-1}.

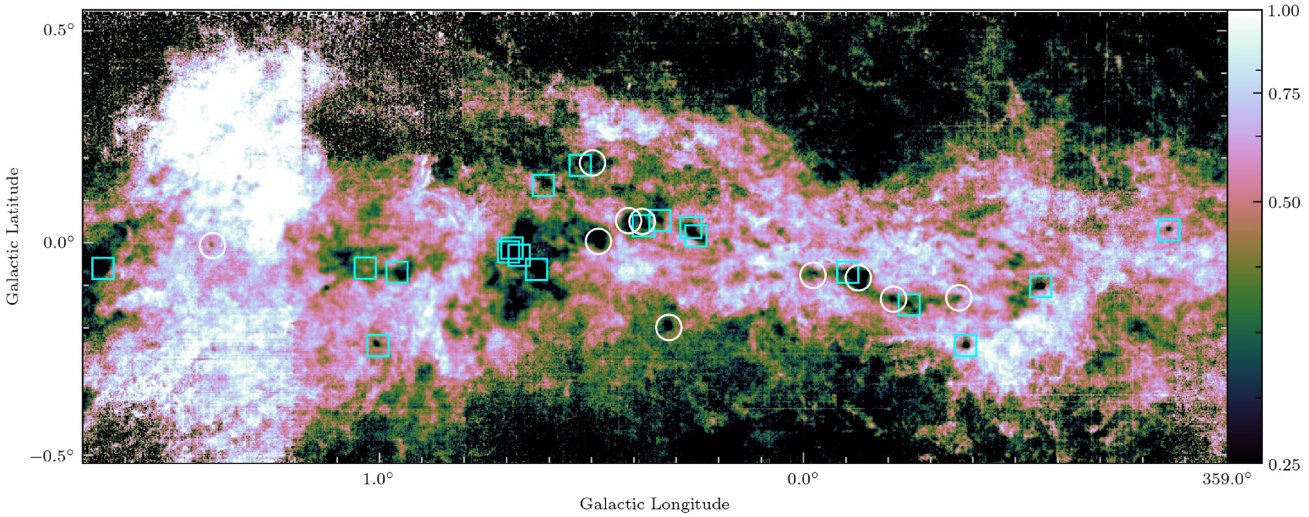

Figure 8. A close-up of the central portion of Panel (d) of Fig. 4. The cyan squares are compact sources detected at 4σ significance using CUTEX. The white circles are at the positions of several known dense clouds or clumps. Both samples are included in Table 4.

Table 4. Known compact sources in the ^{12}CO/500-μm ratio map (Fig. 8). Sources labelled with an asterisk were also detected by CUTEX.

Galactic longitude (°)	Galactic latitude (°)	Source name and notes	Reference
359.137	+0.030	∗H II region; MMB G359.138+00.031	Walsh et al. (1998), Caswell et al. (2010)
359.440	− 0.103	∗Sgr C	Tsuboi et al. (1991)
359.617	− 0.243	∗BGPS G359.617–00.243; MMB G359.615–00.243	Caswell et al. (2010), Rosolowsky et al. (2010)
359.633	− 0.130	BGPS G359.636–00.131	Rosolowsky et al. (2010)
359.750	− 0.147	∗AGAL G359.751–00.144	Contreras et al. (2013)
359.787	− 0.133	JCMT SCUBA source; BGPS G359.788–00.137	Di Francesco et al. (2008), Rosolowsky et al. (2010)
359.870	− 0.083	20-km s^{-1} cloud: UCH II regions and H_2O maser	Downes et al. (1979), Sjouwerman et al. (2002)
359.895	− 0.070	∗AGAL G359.894–00.067	Contreras et al. (2013)
359.977	− 0.077	50-km s^{-1} cloud: UCH II regions and H_2O maser	Ekers et al. (1983), Reid et al. (1988)
0.253	+0.016	∗*The Brick*	Longmore et al. (2012)
0.265	+0.036	∗AGAL G000.264+00.032	Contreras et al. (2013)
0.317	− 0.200	AGAL 0.316–0.201; MMB	Urquhart et al. (2013)
0.338	+0.052	∗Dust-ridge b	Lis et al. (1999)
0.377	+0.040	∗MMB G000.376+00.040; BGPS G000.378+00.041	Caswell et al. (2010), Rosolowsky et al. (2010)
0.380	+0.050	Dust-ridge c	Lis et al. (1999)
0.412	+0.052	Dust-ridge d & BGPS G000.414+00.051	Lis et al. (1999), Rosolowsky et al. (2010)
0.483	+0.003	Sgr B1-off: UCH II regions and H_2O maser	Lu et al. (2019)
0.497	+0.188	MMB G000.496+00.188; BGPS G000.500+00.187	Caswell et al. (2010), Rosolowsky et al. (2010)
0.526	+0.182	∗AGAL 0.526+0.182	Contreras et al. (2013)
0.613	+0.135	∗2MASS J17463693–2820212	Cutri et al. (2003)
0.629	− 0.063	∗AGAL G000.629–00.062	Contreras et al. (2013)
0.670	− 0.030	∗Sgr B2: UCH II regions	Ginsburg et al. (2018)
0.687	− 0.013	∗JCMT SCUBA-2 source	Parsons et al. (2018)
0.695	− 0.022	∗AGAL G000.693–00.026	Contreras et al. (2013)
0.958	− 0.070	∗JCMT SCUBA-2 source	Parsons et al. (2018)
1.003	− 0.243	∗Sgr D1	Liszt (1992)
1.123	− 0.110	∗Sgr D UCHII + H_2O	Downes & Maxwell (1966), Mehringer et al. (1998)
1.393	− 0.007	Sgr D8	Eckart et al. (2006)
1.651	− 0.061	∗ AGAL G001.647–00.062	Contreras et al. (2013)

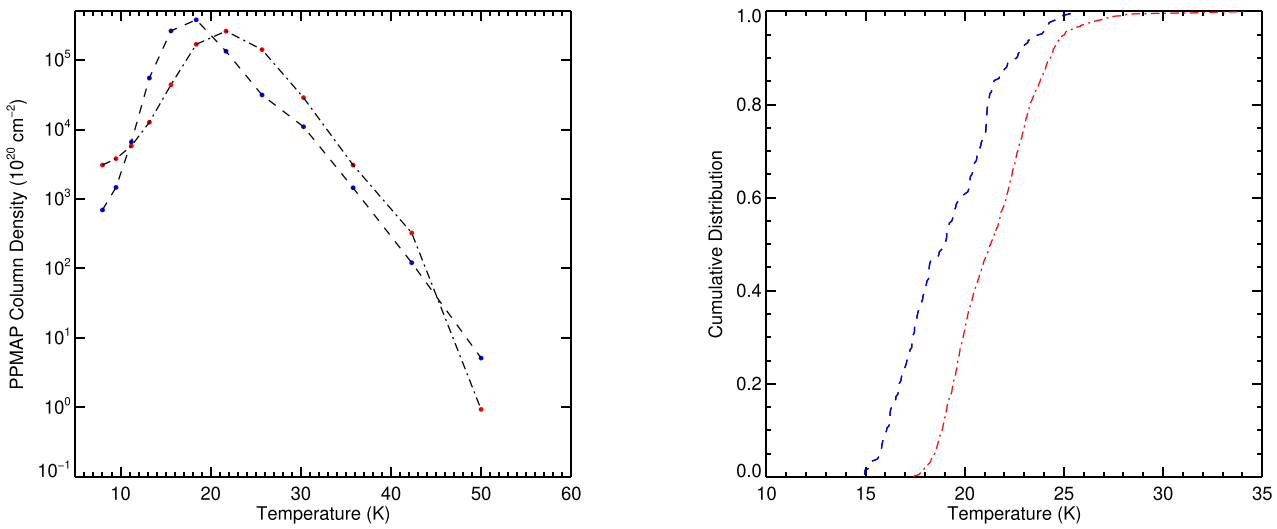

Figure 9. Left-hand panel: The total column density found within the CUTEX sources in each temperature slice from the PPMAP analysis of the CMZ (Marsh et al. 2017). The minima from Fig. 8 are represented by blue points, whereas the maxima are red. Right-hand panel: The cumulative distribution of the temperature contained within the CUTEX in the column-density weighted PPMAP temperature maps. The minima are represented by the blue dashed line, whereas the maxima are the red dot–dashed line.

4.2 Kinematic structure

4.2.1 High-velocity-dispersion features

Fig. 10 contains the $\ell - V_{\rm LSR}$ distribution of the ^{12}CO $J = 3 \rightarrow 2$ intensity, integrated over the whole latitude range. The main features are labelled in Fig. 10 and are the parallelogram-like structure; Bania's Clump 2; the Connecting Arm, the dust lanes fuelling the CMZ; and a series of supernova remnants.

The bright, high-velocity-dispersion emission between $\ell \simeq 358.^{\circ}5$ and $1.^{\circ}5$; $V_{\rm LSR} \sim \pm 250\,{\rm km\,s^{-1}}$ in Fig. 10 that resembles a parallel-

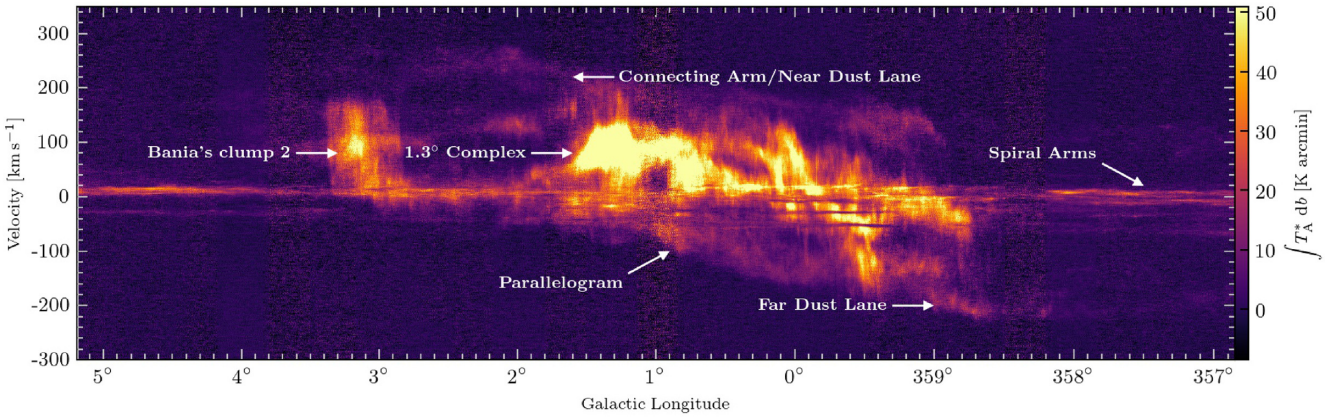

Figure 10. CMZ longitude–velocity map of ^{12}CO $J = 3 \rightarrow 2$ intensity integrated over latitude from data complete as of 2018 September.

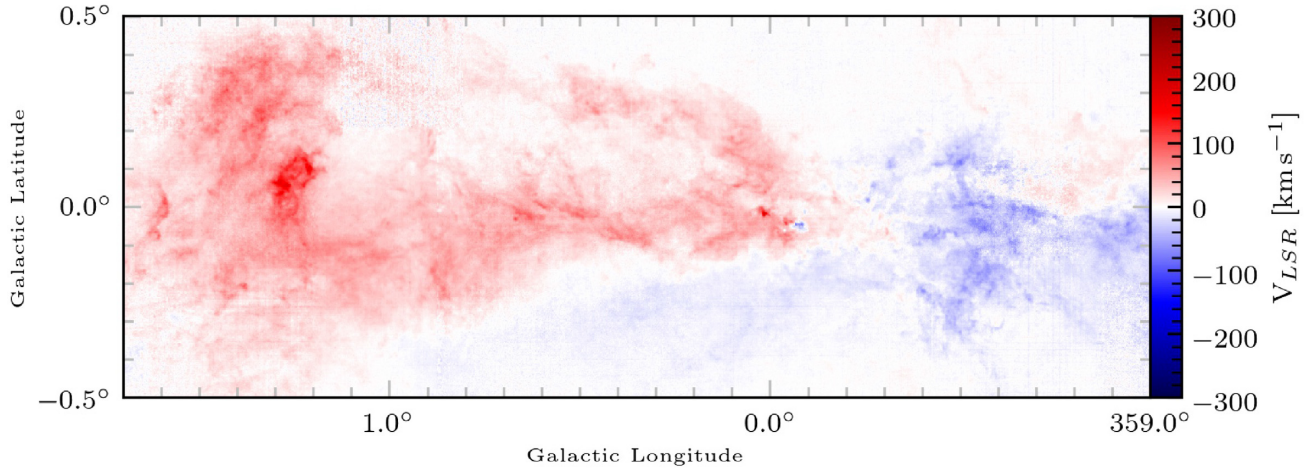

Figure 11. First moment map of the ^{12}CO CMZ map in the region represented in Fig. 8.

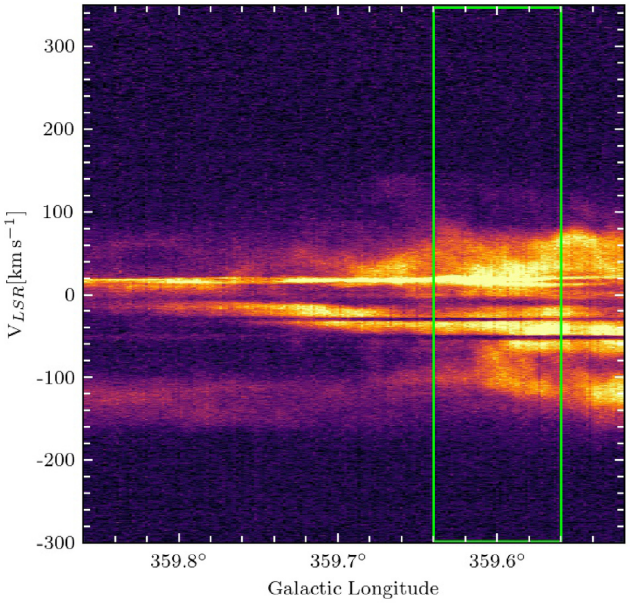

Figure 12. Longitude–velocity map of the individual ^{12}CO tile containing the reported position of the IMBH CO−0.40–0.22 (Oka et al. 2016, 2017). The expected longitude range is marked by the green rectangle.

ogram (Bania 1977; Bally et al. 1987; Morris & Serabyn 1996) is thought to be caused by the dust lanes in the CMZ. The lateral sides are interpreted as the gas that is accreting on to the CMZ from the dust lanes (Sormani et al. 2019). The top and bottom sides are caused by gas that is partly accreting on to the CMZ after travelling past the dust lanes (Sormani et al. 2018). This, combined with the efficient conversion of atomic to molecular gas, causes the velocity structure that we observe in the CMZ (Sormani, Binney & Magorrian 2015a).

The longitudinal asymmetry of this region of bright CO emission with respect to $\ell = 0°$, along with the velocity centroid offset of $\sim$+40 km s^{-1} seen in Fig. 10, was previously explained as the result of gas responding to an asymmetry in the Galactic potential in $m = 1$ mode oscillation with respect to the Galactic disc (e.g. Morris & Serabyn 1996). However, the positional asymmetry has been recently suggested by Sormani et al. (2018) to be due to non-steady flow of gas in the bar potential. In these models, a combination of hydrodynamical and thermal instabilities mean that the gas flow into the CMZ is clumpy and unsteady. This structure leads to transient asymmetries in the inward flow, which we observe, the authors argue, as the longitudinal asymmetry in the gas distribution. Also, structures similar to those observed at the top and bottom edges of the parallelogram feature are detected in the simulations, where they correspond to far- and near-side shocks at the leading edges of the rotating bar. The bright compact structures within this structure are the molecular clouds on librations around x_2 orbits in a ring around

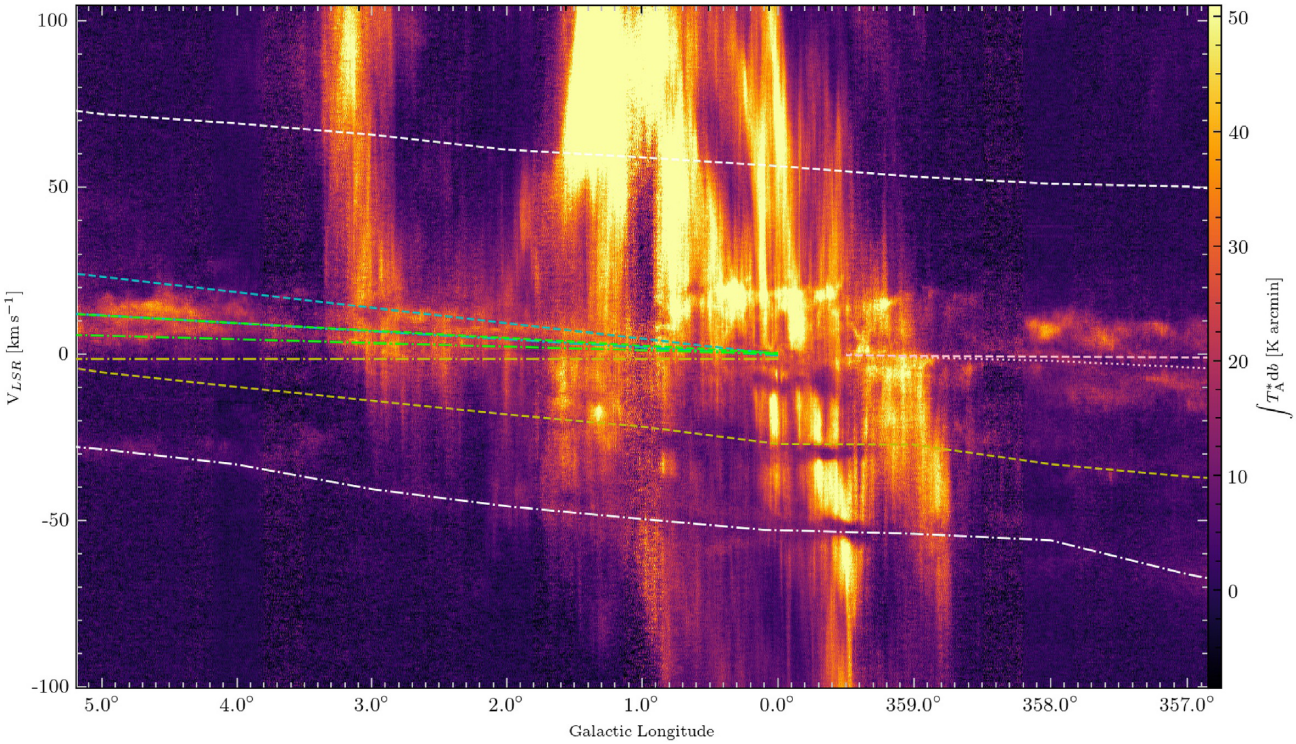

Figure 13. As in Fig. 10 but with the spiral arms of Reid et al. (2016) overlaid and the velocity range restricted to $V_{\rm LSR} \pm 100\,{\rm km\,s^{-1}}$. The arm segments are labelled as follows: 3-kpc near and far arms (3kN, 3kF; white dashed and white dot–dashed, respectively), Carina near portion (CrN; pink dashed), Centaurus-Crux near (CtN; pink dotted), Norma or 4-kpc (Nor; yellow dashed), Outer (Out; yellow dotted), Perseus (Per; blue dotted), Scutum near and far portions (ScN, ScF; blue dot–dashed and blue dashed, respectively), and Sagittarius near and far portions (SgN, SgF; green dot–dashed and green dashed, respectively). The Connecting Arm is out of this velocity range whilst the Outer Scutum-Centaurus, Carina far, an extension of the Connecting Arm, and Centaurus-Crux far arm segments currently have no parallax measurements and are not plotted.

the CMZ with semimajor axis ∼0.3 kpc; and the several features that are narrow in ℓ, but have large velocity dispersions, are shocks where the infalling material meets the CMZ or librations around an x_2 orbit (Kruijssen, Dale & Longmore 2015; Tress et al. 2020). The velocity offset is displayed in Fig. 11. This is the first-moment map of the sub-region in Fig. 8, created using the SPECTRAL-CUBE package (Ginsburg et al. 2019) and reflecting the centroid velocity at each pixel.

Bania's Clump 2 can be seen as a high-velocity-dispersion cloud in Fig. 10 at $\ell = 3.^{\circ}2$ (Bania 1977). The line width of Bania's Clump 2 appears to cover over 100 km s^{-1} (Stark & Bania 1986), with very narrow longitude coverage (Liszt 2006) but high-resolution data have found that the velocity range is made up of many lower linewidth components (Longmore et al. 2017). Clouds such as these are the signature of shocks as clouds collide with the dust lane, as opposed to the turbulence of individual clouds (Sormani, Binney & Magorrian 2015b; Sormani et al. 2019). Another high-velocity-dispersion cloud present in Fig. 10 is the $\ell = 1.^{\circ}3$ complex (Bally et al. 1988; Oka et al. 1998). The high-velocity dispersion has three potential causes. The first is a series of supernova explosions (Tanaka et al. 2007), with the alternatives reflecting the acceleration of gas flows along magnetic field lines due to Parker instabilities (Suzuki et al. 2015; Kakiuchi et al. 2018) or collisions between gas on the dust lanes and the gas orbiting the CMZ (Sormani et al. 2019). Neither of these two structures shows signatures of ongoing star formation (Tanaka et al. 2007; Bally et al. 2010), with no associated 70-μm Hi-GAL compact sources (Elia et al. 2017), which are considered to be a signature of active star formation (Ragan et al. 2016, 2018).

The Connecting Arm (Rodriguez-Fernandez et al. 2006) is also visible in the $\ell - V_{\rm LSR}$ diagram. Though described as a spiral arm, it is in fact a dust lane at the near side of the CMZ (e.g. Fux 1999; Marshall et al. 2008; Sormani et al. 2018), with a symmetrical dust lane found at the far side of the CMZ. We also see the latter in Fig. 10 as the curved feature at $V_{\rm LSR} \sim -200\,{\rm km\,s^{-1}}$ running between $\ell \simeq 359^{\circ}$ and 357°. These dust lanes are signatures of accretion into the CMZ (Sormani & Barnes 2019), fuelling episodic star formation in this region (Krumholz et al. 2017).

We also confirm the findings of Tanaka (2018), who observed no evidence of an intermediate-mass black hole (IMBH) at the position of $\ell = -0.^{\circ}40$, $b = -0.^{\circ}22$ (Oka et al. 2016, 2017). Fig. 12 shows the $\ell - V_{\rm LSR}$ ^{12}CO intensity distribution of the observed tile that would contain this IMBH. There are no large-velocity-dispersion features that are indicative of an accreting IMBH being present in the $\ell - V_{\rm LSR}$ maps.

4.2.2 *Foreground features*

The $\ell - V_{\rm LSR}$ plot (Fig. 10) also shows several clear features with narrow velocity widths, in absorption and emission, probably corresponding to foreground structures, namely spiral arms. We can use these features to constrain the loci of these arms as they cross the CMZ. Several of the arm features modelled in Reid et al. (2016) are plotted on the same data, restricted to $V_{\rm LSR} \pm 100\,{\rm km\,s^{-1}}$, in Fig. 13.

At the $\ell = 0^{\circ}$ position, there are three features in absorption at $V_{\rm LSR} \simeq -60$, -30 and $-10\,{\rm km\,s^{-1}}$, with one emission feature at $\sim +10\,{\rm km\,s^{-1}}$. All of these appear to have substructure and

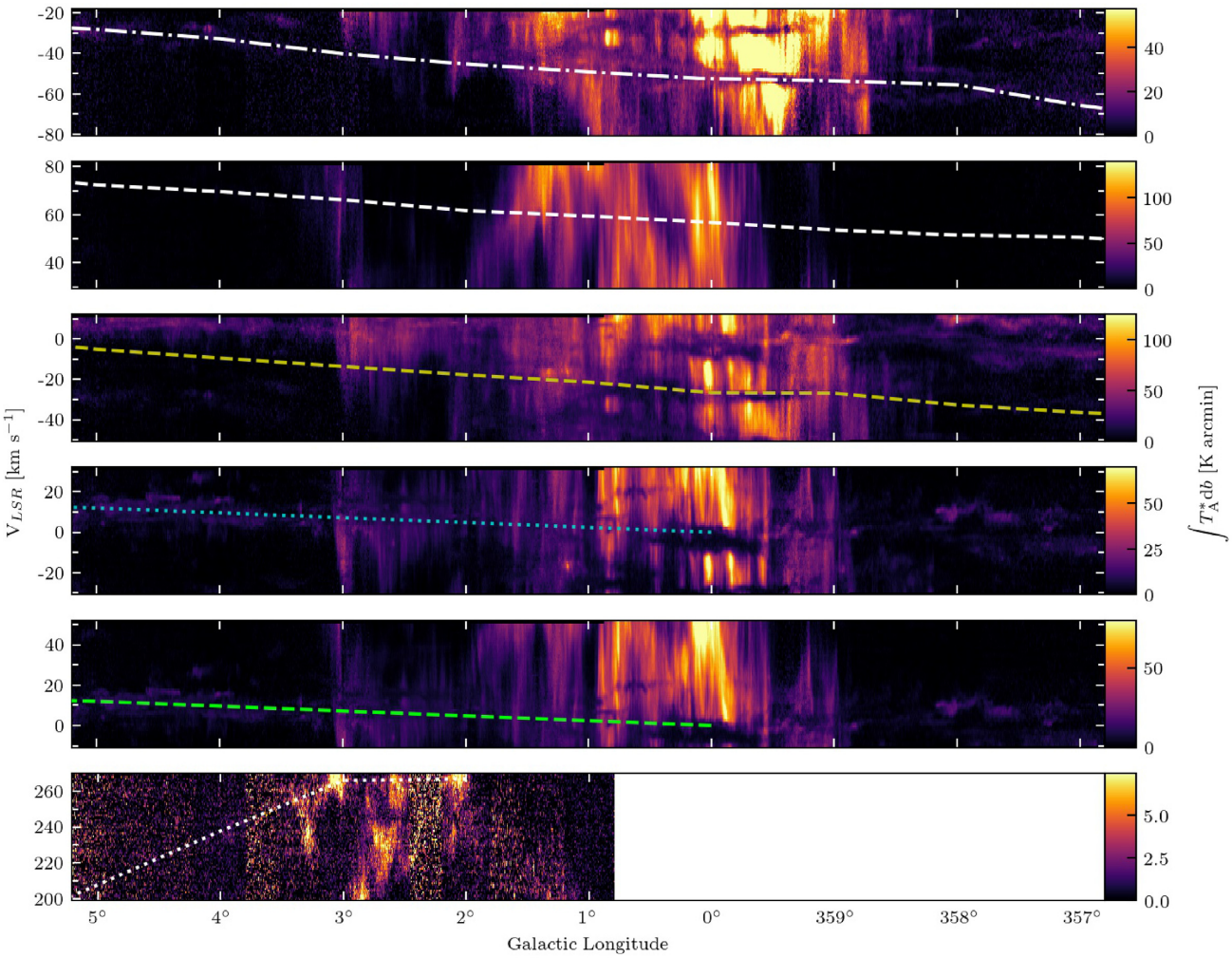

Figure 14. Longitude–velocity maps isolated over the latitude and velocity range identified by Reid et al. (2016). Top panel: near 3-kpc arm. Second panel: far 3-kpc arm. Third panel: Norma spiral arms. Fourth panel: Perseus spiral arm. Fifth panel: far Sagittarius spiral arm. Bottom panel: Connecting Arm, which is limited to a longitude range of $\ell > 0.^\circ 8$. The overlaid lines are the loci of the relevant spiral arms.

possibly shallow gradients and are somewhat discontinuous across the longitude range. Following Bronfman et al. (2000) and Sanna et al. (2014), we can postulate that the $-60\,\mathrm{km\,s^{-1}}$ feature is the near 3-kpc arm and the $-30\,\mathrm{km\,s^{-1}}$ feature is the Norma arm.

To identify these features, more-precise $\ell - V_{\mathrm{LSR}}$ plots were made, integrating over the latitude and velocity range identified for these arms in Reid et al. (2016). Fig. 14 displays the $\ell - V_{\mathrm{LSR}}$ plots for the near 3-kpc arm, far 3-kpc arm, Norma arm, Perseus arm, and the far Sagittarius arm. The latitude and velocity ranges of the five spiral arms are: $\pm 0.^\circ 2$ and -80 to $-20\,\mathrm{km\,s^{-1}}$, $\pm 0.^\circ 1$ and 30 to $80\,\mathrm{km\,s^{-1}}$, $\pm 0.^\circ 2$ and -50 to $10\,\mathrm{km\,s^{-1}}$, $-0.^\circ 1$ to 0° and -30 to $30\,\mathrm{km\,s^{-1}}$, and $-0.^\circ 1$ to 0° and -10 to $50\,\mathrm{km\,s^{-1}}$, for the near 3-kpc, far 3-kpc, Norma, Perseus, and far Sagittarius arms, respectively.

The $\ell - V_{\mathrm{LSR}}$ plots for the near 3-kpc arm and the Norma arm confirm the detection of these spiral arms. The near-3kpc arm displays absorption in the CMZ region, with emission detected in positive longitudes. The Norma spiral arm is detected in absorption. There is no evidence in these data of the far 3-kpc arm, that Sanna et al. (2014) suggest crosses $\ell = 0^\circ$ at $+56\,\mathrm{km\,s^{-1}}$.

The Perseus spiral arm and the far segment of the Sagittarius arm both have emission that corresponds to the loci of these arms, in the positive longitudes at velocities $V_{\mathrm{LSR}} \simeq +10\,\mathrm{km\,s^{-1}}$. We are therefore unable to confirm which of these spiral arms we have detected.

We have also produced the $\ell - V_{\mathrm{LSR}}$ plot for the Connecting Arm, using the Reid et al. (2016) latitude and velocity ranges of $-0.^\circ 5$ to $0.^\circ 3$ and 200 to $270\,\mathrm{km\,s^{-1}}$. We detect this structure, the near-side dust lane down which material streams from distances of 3 kpc into the CMZ (e.g. Cohen & Davies 1976; Rodriguez-Fernandez et al. 2006; Sormani & Barnes 2019).

In future work, we will extract the detected narrow arm features from the ^{12}CO data cubes in order to analyse the molecular-gas properties within them and to allow kinematic analysis of the kinematics of the residual high-velocity-dispersion emission in the CMZ itself.

5 SUMMARY

We introduce the CO Heterodyne Inner Milky Way Plane Survey (CHIMPS2). CHIMPS2 will complement the CHIMPS (Rigby et al. 2016) and COHRS (Dempsey et al. 2013) surveys by observing the CMZ, a segment of the Outer Galaxy, and to connect the CMZ to the current CHIMPS and COHRS observations in ^{12}CO, ^{13}CO, and C^{18}O ($J = 3 \rightarrow 2$) emission.

We present the ^{12}CO $J = 3 \rightarrow 2$ data in the CMZ, covering approximately $-3^\circ \leq \ell \leq 5^\circ$ and $|\, b \,| \leq 0.^\circ 50$. The data have a spatial resolution of 15 arcsec, a spectral resolution of 1 km s^{-1} over velocities of $|\ V_{\rm LSR}\ | \leq 300$ km s^{-1}, an rms of 0.58 K on 7.5 arcsec pixels and are available to download from the CANFAR archive.

Taking the ratio of the integrated-intensity to the 500-μm continuum surface brightness from Hi-GAL, we find that the result correlates well with dust temperature. The minima tend to coincide with compact, dense, cool sources; whereas the maxima correspond to warmer, more-extended regions.

We investigate the kinematic structure of the CMZ data through the use of $\ell - V_{\rm LSR}$ plots. We are able to distinguish the high-velocity-dispersion features in the Galactic Centre, such as Bania's Clump 2. We find no evidence for the existence of IMBHs. We find evidence for spiral arms crossing in front of the Galactic Centre in both absorption and emission, detecting the near 3-kpc spiral arm, along with the Norma spiral arm, and evidence for emission in the space occupied by the far Sagittarius arm and the Perseus arm.

These data provide high-resolution observations of molecular gas in the CMZ, and will be a valuable data set for future CMZ studies, especially when combined with the future ^{13}CO and C^{18}O CHIMPS2 data. Further combination with the complimentary data sets from existing surveys in the molecular gas, such as SEDIGISM, and in the continuum from Hi-GAL and ATLASGAL will further increase the value.

ACKNOWLEDGEMENTS

We would like to thank the anonymous referee for their comments which have improved the clarity of the paper. DJE is supported by an STFC postdoctoral grant (ST/R000484/1). The James Clerk Maxwell Telescope is operated by the East Asian Observatory on behalf of The National Astronomical Observatory of Japan; Academia Sinica Institute of Astronomy and Astrophysics; the Korea Astronomy and Space Science Institute; the Operation, Maintenance, and Upgrading Fund for Astronomical Telescopes and Facility Instruments, budgeted from the Ministry of Finance (MOF) of China and administrated by the Chinese Academy of Sciences (CAS), as well as the National Key Research and Development Program of China (No. 2017YFA0402700). Additional funding support is provided by the Science and Technology Facilities Council of the United Kingdom and participating universities in the United Kingdom and Canada. The Starlink software (Currie et al. 2014) is currently supported by the East Asian Observatory. This research has made use of NASA's Astrophysics Data System. MJC thanks Peter Chiu (RAL Space) for system-administrative support for the server where the data were reduced. GJW gratefully acknowledges the receipt of an Emeritus Fellowship from the Leverhulme Trust. HM and YG are supported by National Natural Science Foundation of China (NSFC) grant nos. U1731237 and 11773054. CWL is supported by the Basic Science Research Program through the National Research Foundation of Korea (NRF) funded by the Ministry of Education, Science and Technology (NRF-2019R1A2C1010851). TL is supported by international partnership program of Chinese Academy of Sciences grant no. 114231KYSB20200009.

DATA AVAILABILITY

The reduced CHIMPS2 ^{12}CO CMZ data are available to download from the CANFAR archive.[2] The data are available as mosaics, roughly $2^\circ \times 1^\circ$ in size, as well as the individual observations. Integrated $\ell - b$ and $\ell - V_{\rm LSR}$ maps, displayed in Section 5 for the whole CMZ are provided, as well as the $\ell - V_{\rm LSR}$ maps for the individual cubes. The data are presented in FITS format.

The raw data are also downloadable from the JCMT Science Archive[3] hosted by the Canadian Astronomy Data Centre using the Project ID M17BL004.

REFERENCES

André P. et al., 2010, A&A, 518, L102
Armillotta L., Krumholz M. R., Di Teodoro E. M., McClure-Griffiths N. M., 2019, MNRAS, 490, 4401
Bally J., Stark A. A., Wilson R. W., Henkel C., 1987, ApJS, 65, 13
Bally J., Stark A. A., Wilson R. W., Henkel C., 1988, ApJ, 324, 223
Bally J. et al., 2010, ApJ, 721, 137
Bania T. M., 1977, ApJ, 216, 381
Barnes P. J., Muller E., Indermuehle B., O'Dougherty S. N., Lowe V., Cunningham M., Hernandez A. K., Fuller G. A., 2015, ApJ, 812, 6
Benedettini M. et al., 2020, A&A, 633, A147
Beuther H. et al., 2016, A&A, 595, A32
Bialy S., Bihr S., Beuther H., Henning T., Sternberg A., 2017, ApJ, 835, 126
Bronfman L., Casassus S., May J., Nyman L.-Å., 2000, A&A, 358, 521
Brunt C. M., Federrath C., 2014, MNRAS, 442, 1451
Buckle J. V. et al., 2009, MNRAS, 399, 1026
Caswell J. L. et al., 2010, MNRAS, 404, 1029
Chapin E., Gibb A. G., Jenness T., Berry D. S., Scott D., Tilanus R. P. J., 2013, Starlink User Note 258, the Sub-Millimetre User Reduction Facility. Joint Astronomy Centre
Cohen R. J., Davies R. D., 1976, MNRAS, 175, 1
Contreras Y. et al., 2013, A&A, 549, A45
Currie M. J., Berry D. S., Jenness T., Gibb A. G., Bell G. S., Draper P. W., 2014, in Manset N., Forshay P., eds, ASP Conf. Ser. Vol. 485, Astronomical Data Analysis Software and Systems XXIII. Astron. Soc. Pac., San Francisco, p. 391
Curtis E. I., Richer J. S., Buckle J. V., 2010, MNRAS, 401, 455
Cutri R. M. et al., 2003, The IRSA 2MASS All-Sky Point Source Catalog, available at http://irsa.ipac.caltech.edu/applications/Gator/
Dame T. M., Hartmann D., Thaddeus P., 2001, ApJ, 547, 792
Dempsey J. T., Thomas H. S., Currie M. J., 2013, ApJS, 209, 8
Dib S., Helou G., Moore T. J. T., Urquhart J. S., Dariush A., 2012, ApJ, 758, 125
Di Francesco J., Johnstone D., Kirk H., MacKenzie T., Ledwosinska E., 2008, ApJS, 175, 277
Downes D., Maxwell A., 1966, ApJ, 146, 653
Downes D., Goss W. M., Schwarz U. J., Wouterloot J. G. A., 1979, A&AS, 35, 1
Eckart A. et al., 2006, A&A, 450, 535
Eden D. J., Moore T. J. T., Plume R., Morgan L. K., 2012, MNRAS, 422, 3178
Eden D. J., Moore T. J. T., Morgan L. K., Thompson M. A., Urquhart J. S., 2013, MNRAS, 431, 1587
Eden D. J., Moore T. J. T., Urquhart J. S., Elia D., Plume R., Rigby A. J., Thompson M. A., 2015, MNRAS, 452, 289
Eden D. J. et al., 2017, MNRAS, 469, 2163
Ekers R. D., van Gorkom J. H., Schwarz U. J., Goss W. M., 1983, A&A, 122, 143
Elia D. et al., 2013, ApJ, 772, 45
Elia D. et al., 2017, MNRAS, 471, 100
Elmegreen D. M., 1980, ApJ, 242, 528
Federrath C. et al., 2016, ApJ, 832, 143
Fux R., 1999, A&A, 345, 787
Gao Y., Solomon P. M., 2004, ApJ, 606, 271

[2] https://www.canfar.net/citation/landing?doi=20.0004

[3] http://www.cadc-ccda.hia-iha.nrc-cnrc.gc.ca/en/jcmt/

Ginsburg A. et al., 2018, ApJ, 853, 171
Ginsburg A. et al. , 2019, radio-astro-tools/spectral-cube: v0.4.4. Zenodo, available at https://zenodo.org/record/2573901#.X29DAtkzaM8
Gong Y. et al., 2016, A&A, 588, A104
Henshaw J. D. et al., 2016, MNRAS, 457, 2675
James P. A., Percival S. M., 2016, MNRAS, 457, 917
James P. A., Percival S. M., 2018, MNRAS, 474, 3101
Jenness T., Economou F., 2015, Astron. Comput., 9, 40
Jenness T., Chapin E. L., Berry D. S., Gibb A. G., Tilanus R. P. J., Balfour J., Tilanus V., Currie M. J., 2013, Astrophysics Source Code Library, record ascl:1310.007
Jenness T., Currie M. J., Tilanus R. P. J., Cavanagh B., Berry D. S., Leech J., Rizzi L., 2015, MNRAS, 453, 73
Kakiuchi K., Suzuki T. K., Fukui Y., Torii K., Enokiya R., Machida M., Matsumoto R., 2018, MNRAS, 476, 5629
Kendrew S. et al., 2012, ApJ, 755, 71
Kennicutt R. C., Jr, 1998, ApJ, 498, 541
Kruijssen J. M. D., Longmore S. N., 2013, MNRAS, 435, 2598
Kruijssen J. M. D., Longmore S. N., 2014, MNRAS, 439, 3239
Kruijssen J. M. D., Longmore S. N., Elmegreen B. G., Murray N., Bally J., Testi L., Kennicutt R. C., 2014, MNRAS, 440, 3370
Kruijssen J. M. D., Dale J. E., Longmore S. N., 2015, MNRAS, 447, 1059
Krumholz M. R., Kruijssen J. M. D., Crocker R. M., 2017, MNRAS, 466, 1213
Lada C. J., Forbrich J., Lombardi M., Alves J. F., 2012, ApJ, 745, 190
Lis D. C., Li Y., Dowell C. D., Menten K. M., 1999, in Cox P., Kessler M., eds, ESA SP-427: The Universe as Seen by ISO. ESA, Noordwijk, p. 627
Liszt H. S., 1992, ApJS, 82, 495
Liszt H. S., 2006, A&A, 447, 533
Liu T. et al., 2018, ApJS, 234, 28
Longmore S. N. et al., 2012, ApJ, 746, 117
Longmore S. N. et al., 2013, MNRAS, 429, 987
Longmore S. N. et al., 2017, MNRAS, 470, 1462
Lu X. et al., 2019, ApJ, 872, 171
Marsh K. A., Whitworth A. P., Lomax O., 2015, MNRAS, 454, 4282
Marsh K. A. et al., 2017, MNRAS, 471, 2730
Marshall D. J., Fux R., Robin A. C., Reylé C., 2008, A&A, 477, L21
Mehringer D. M., Goss W. M., Lis D. C., Palmer P., Menten K. M., 1998, ApJ, 493, 274
Minamidani T. et al., 2016, in Holland W. S., Zmuidzinas J., eds, Proc. SPIE Conf. Ser. Vol. 9914, Millimeter, Submillimeter, and Far-Infrared Detectors and Instrumentation for Astronomy VIII. SPIE, Bellingham. p. 99141Z
Molinari S. et al., 2010a, PASP, 122, 314
Molinari S. et al., 2010b, A&A, 518, L100
Molinari S., Schisano E., Faustini F., Pestalozzi M., di Giorgio A. M., Liu S., 2011a, A&A, 530, A133
Molinari S. et al., 2011b, ApJ, 735, L33
Molinari S. et al., 2016, A&A, 591, A149
Molinari S., Schisano E., Faustini F., Pestalozzi M., di Giorgio A. M., Liu S., 2017, Astrophysics Source Code Library, record ascl:1708.018
Moore T. J. T., Urquhart J. S., Morgan L. K., Thompson M. A., 2012, MNRAS, 426, 701
Moore T. J. T. et al., 2015, MNRAS, 453, 4264
Morris M., Serabyn E., 1996, ARA&A, 34, 645
Nishimura A. et al., 2015, ApJS, 216, 18
Oka T., Hasegawa T., Sato F., Tsuboi M., Miyazaki A., 1998, ApJS, 118, 455
Oka T., Onodera Y., Nagai M., Tanaka K., Matsumura S., Kamegai K., 2012, ApJS, 201, 14
Oka T., Mizuno R., Miura K., Takekawa S., 2016, ApJ, 816, L7
Oka T., Tsujimoto S., Iwata Y., Nomura M., Takekawa S., 2017, Nat. Astron., 1, 709
Onodera S. et al., 2010, ApJ, 722, L127
Orkisz J. H. et al., 2017, A&A, 599, A99
Parsons H. et al., 2018, ApJS, 234, 22
Peñaloza C. H., Clark P. C., Glover S. C. O., Shetty R., Klessen R. S., 2017, MNRAS, 465, 2277
Peñaloza C. H., Clark P. C., Glover S. C. O., Klessen R. S., 2018, MNRAS, 475, 1508
Planck Collaboration XI, 2014, A&A, 571, A11
Ragan S. E., Henning T., Tackenberg J., Beuther H., Johnston K. G., Kainulainen J., Linz H., 2014, A&A, 568, A73
Ragan S. E., Moore T. J. T., Eden D. J., Hoare M. G., Elia D., Molinari S., 2016, MNRAS, 462, 3123
Ragan S. E., Moore T. J. T., Eden D. J., Hoare M. G., Urquhart J. S., Elia D., Molinari S., 2018, MNRAS, 479, 2361
Reid M. J., Schneps M. H., Moran J. M., Gwinn C. R., Genzel R., Downes D., Roennaeng B., 1988, ApJ, 330, 809
Reid M. J., Dame T. M., Menten K. M., Brunthaler A., 2016, ApJ, 823, 77
Rigby A. J. et al., 2016, MNRAS, 456, 2885
Rigby A. J. et al., 2019, A&A, 632, A58
Rodriguez-Fernandez N. J., Combes F., Martin-Pintado J., Wilson T. L., Apponi A., 2006, A&A, 455, 963
Rosolowsky E. et al., 2010, ApJS, 188, 123
Sanna A. et al., 2014, ApJ, 781, 108
Schinnerer E. et al., 2017, ApJ, 836, 62
Schisano E. et al., 2014, ApJ, 791, 27
Schruba A., Leroy A. K., Walter F., Sandstrom K., Rosolowsky E., 2010, ApJ, 722, 1699
Schuller F. et al., 2017, A&A, 601, A124
Sjouwerman L. O., Lindqvist M., van Langevelde H. J., Diamond P. J., 2002, A&A, 391, 967
Smartt S. J., Rolleston W. R. J., 1997, ApJ, 481, L47
Sofue Y., Nakanishi H., 2016, PASJ, 68, 63
Sormani M. C., Barnes A. T., 2019, MNRAS, 484, 1213
Sormani M. C., Binney J., Magorrian J., 2015a, MNRAS, 449, 2421
Sormani M. C., Binney J., Magorrian J., 2015b, MNRAS, 454, 1818
Sormani M. C., Treß R. G., Ridley M., Glover S. C. O., Klessen R. S., Binney J., Magorrian J., Smith R., 2018, MNRAS, 475, 2383
Sormani M. C. et al., 2019, MNRAS, 488, 4663
Sormani M. C., Tress R. G., Glover S. C. O., Klessen R. S., Battersby C. D., Clark P. C., Hatchfield H. P., Smith R. J., 2020, MNRAS, 497, 5024
Stark A. A., Bania T. M., 1986, ApJ, 306, L17
Stark A. A., Lee Y., 2006, ApJ, 641, L113
Su Y. et al., 2019, ApJS, 240, 9
Suwannajak C., Tan J. C., Leroy A. K., 2014, ApJ, 787, 68
Suzuki T. K., Fukui Y., Torii K., Machida M., Matsumoto R., 2015, MNRAS, 454, 3049
Szűcs L., Glover S. C. O., Klessen R. S., 2014, MNRAS, 445, 4055
Tanaka K., 2018, ApJ, 859, 86
Tanaka K., Kamegai K., Nagai M., Oka T., 2007, PASJ, 59, 323
Thompson M. A., Urquhart J. S., Moore T. J. T., Morgan L. K., 2012, MNRAS, 421, 408
Tress R. G., Sormani M. C., Glover S. C. O., Klessen R. S., Battersby C. D., Clark P. C., Hatchfield H. P., Smith R. J., 2020, preprint (arXiv: 2004.06724)
Tsuboi M., Kobayashi H., Ishiguro M., Murata Y., 1991, PASJ, 43, L27
Umemoto T. et al., 2017, PASJ, 69, 78
Urquhart J. S. et al., 2013, MNRAS, 431, 1752
Urquhart J. S. et al., 2014, A&A, 568, A41
Urquhart J. S. et al., 2018, MNRAS, 473, 1059
Urquhart J. S. et al., 2020, MNRAS, in press
Walker D. L. et al., 2018, MNRAS, 474, 2373
Walsh A. J., Burton M. G., Hyland A. R., Robinson G., 1998, MNRAS, 301, 640
Wang Y. et al., 2020, A&A, 634, A83
Yusef-Zadeh F. et al., 2009, ApJ, 702, 178
Zucker C., Battersby C., Goodman A., 2015, ApJ, 815, 23

APPENDIX A: ORAC-DR PARAMETERS

The available recipe parameters are described in the REDUCE_SCIENCE_NARROWLINE documentation and summarized

in the *Classified Recipe Parameters* appendix of Starlink Cookbook 20.[4]

We first list the parameters that were constant throughout the survey and will be applied to all ^{12}CO data in the CHIMPS2 survey. The following parameters controlled the creation of the spectral cubes with SMURF:MAKECUBE (Chapin et al. 2013; Jenness et al. 2013), and the maximum size of input data before they were processed in chunks.

```
CUBE_WCS = GALACTIC
PIXEL_SCALE = 6.0
SPREAD_METHOD = gauss
SPREAD_WIDTH = 9
SPREAD_FWHM_OR_ZERO = 6
TILE = 0
CUBE_MAXSIZE = 1536

CHUNKSIZE = 12288
```

The following parameters controlled the creation of the longitude–velocity maps and spectral-channel re-binning for the tiling of a large number of tiles.

```
REBIN = 1.0
LV_IMAGE = 1
LV_AXIS = skylat
LV_ESTIMATOR = sum
```

To guide the automated rejection of spectra affected by artefacts extraneous noise the following parameters were used.

```
BASELINE_LINEARITY = 1
BASELINE_LINEARITY_LINEWIDTH = base
BASELINE_REGIONS = −406.8:-272.0,124.0:377.5
BASELINE_LINEARITY_MINRMS = 0.080
HIGHFREQ_INTERFERENCE = 1
HIGHFREQ_RINGING = 0
LOWFREQ_INTERFERENCE = 1
LOWFREQ_INTERFERENCE_THRESH_CLIP = 4.0
```

These too were constants, except BASELINE_LINEARITY_LINEWIDTH was sometimes set to a range to be excluded from the non-linearity tests if there was a single continuous section of emission, otherwise BASELINE_REGIONS was used inclusively. HIGHFREQ_RINGING was only enabled (set to 1) when ringing (Jenness et al. 2015) was present in HARP Receptor H07. LOWFREQ_INTERFERENCE_THRESH_CLIP was set higher – 6, 8, or 10 – as needed for ^{12}CO observations in the CMZ.

The following three parameters controlled how the receptor-to-receptor flat-field was to be determined. The responses are normalized to Receptor H05, except in 15 cases in where H05 had failed quality-assurance criteria and H10 was substituted. In three CMZ cases the index method was preferred, using well-determined flat ratios from the same night. The regions used to derive the flat-field were estimated by averaging all the spectra in the first pass of a reduction, then tuning through border velocity channels until there was deemed to be sufficient signal that was not overly concentrated, typically when the mean flux exceeded 0.2 K.

```
FLATFIELD = 1
FLAT_METHOD = sum
FLAT_REGIONS = −87.0:54.0,90.0:190.0
```

For ^{12}CO observations in the CMZ, the following parameters related to the baseline fitting were used.

```
BASELINE_METHOD = auto
BASELINE_ORDER = 1
FREQUENCY_SMOOTH = 25
BASELINE_NUMBIN = 128
BASELINE_EMISSION_CLIP = 1.0,1.3,1.6,2.0,2.5
```

In some cases the baseline order was required to be set to 4.

```
BASELINE_ORDER = 4
```

The velocity coverage of the output data products in the CMZ were determined to be −407 to 355, and assigned to the FINAL_LOWER_VELOCITY and FINAL_UPPER_VELOCITY parameters.

The velocity limits containing all identified emission with a margin for error were set by MOMENTS_LOWER_VELOCITY and MOMENTS_UPPER_VELOCITY to aid in the creation of moments' maps, such the integrated emission.

The final set of parameters were only applicable when there was noticeable contamination from the reference (off-position).

```
CLUMP_METHOD = clumpfind
SUBTRACT_REF_EMISSION = 1
REF_EMISSION_MASK_SOURCE = both
REF_EMISSION_COMBINE_REFPOS = 1
REF_EMISSION_BOXSIZE = 19
```

[4]http://www.starlink.ac.uk/devdocs/sc20.htx/sc20.html

[1]*Astrophysics Research Institute, Liverpool John Moores University, IC2, Liverpool Science Park, 146 Brownlow Hill, Liverpool L3 5RF, UK*
[2]*East Asian Observatory, 660 North A'ohoku Place, Hilo, HI 96720, USA*
[3]*RAL Space, STFC Rutherford Appleton Laboratory, Chilton, Didcot, Oxfordshire OX11 0QX, UK*
[4]*School of Physics and Astronomy, Cardiff University, Queen's Buildings, The Parade, Cardiff CF24 3AA, UK*
[5]*Department of Physics, University of Alberta, Edmonton, AB T6G 2R3, Canada*
[6]*Purple Mountain Observatory and Key Laboratory of Radio Astronomy, Chinese Academy of Sciences, Nanjing 210034, People's Republic of China*
[7]*Korea Astronomy and Space Science Institute, 776 Daedeokdae-ro, Yuseong-gu, Daejeon 34055, Republic of Korea*
[8]*University of Science and Technology, Korea (UST), 217 Gajeong-ro, Yuseong-gu, Daejeon 34113, Republic of Korea*
[9]*European Southern Observatory, Karl-Schwarzschild-Strasse 2, D-85748 Garching bei München, Germany*
[10]*Department of Physics, Institute of Astronomy, National Tsing Hua University, 300 Hsinchu, Taiwan*
[11]*Nobeyama Radio Observatory, National Astronomical Observatory of Japan, National Institutes of Natural Sciences, 462-2, Nobeyama, Minamimaki, Minamimaksu, Nagano 384-1305, Japan*
[12]*Department of Astronomical Science, School of Physical Science, SOKENDAI (The Graduate University for Advanced Studies), 2-21-1, Osawa, Mitaka, Tokyo 181-8588, Japan*
[13]*Centre for Astrophysics and Planetary Science, University of Kent, Canterbury CT2 7NH, UK*
[14]*Department of Physics & Astronomy, Kwantlen Polytechnic University, 12666 72nd Avenue, Surrey, BC V3W 2M8, Canada*
[15]*Wartburg College, Waverly, IA 50677, USA*
[16]*Subaru Telescope, National Astronomical Observatory of Japan, National Institutes of Natural Sciences, 650 North A'ohoku Place, Hilo, HI 96720, USA*

[17]*Centre de Recherche en Astrophysique du Québec, Département de Physique, de génie Physique et d'optique, Université Laval, Montreal, QC G1K 7P4, Canada*
[18]*Key Laboratory for Research in Galaxies and Cosmology, Shanghai Astronomical Observatory, Chinese Academy of Sciences, 80 Nandan Road, Shanghai 200030, People's Republic of China*
[19]*Department of Astrophysics, Vietnam National Space Center (VNSC), Vietnam Academy of Science and Technology (VAST), 18 Hoang Quoc Viet, Ha Noi, Vietnam*
[20]*School of Space Research, Kyung Hee University, 1732 Deogyeong-daero, Giheung-gu, Yongin-si, Gyeonggi-do 17104, Republic of Korea*
[21]*SUPA, School of Physics and Astronomy, University of St Andrews, North Haugh, St Andrews KY16 9SS, UK*
[22]*National Astronomical Observatories, Chinese Academy of Sciences, 20A Datun Road, Chaoyang District, Beijing 100012, China*
[23]*Key Laboratory of FAST, NAOC, Chinese Academy of Science, Beijing 100012, China*
[24]*Max-Planck-Institut für Astronomie, Königstuhl 17, D-69117 Heidelberg, Germany*
[25]*Division of Particle and Astrophysical Science, Graduate School of Science, Nagoya University, Furo-cho, Chikusa-ku, Nagoya, Aichi 464-8602, Japan*
[26]*Department of Earth and Space Science, Graduate School of Science, Osaka University, 1-1, Machikaneyama-cho, Toyonaka, Osaka 560-0043, Japan*
[27]*Astronomical Institute, Graduate School of Science, Tohoku University, Aoba, Sendai, Miyagi 980-8578, Japan*
[28]*Centre for Astrophysics Research, School of Physics Astronomy & Mathematics, University of Hertfordshire, College Lane, Hatfield, Herts AL10 9AB, UK*
[29]*SUPA, School of Science and Engineering, University of Dundee, Nethergate, Dundee DD1 4HN, UK*
[30]*Department of Physics and Astronomy, University of Waterloo, Waterloo, ON N2L 3G1, Canada*
[31]*Department of Astronomy, Xiamen University, Xiamen, Fujian 361005, China*
[32]*Institute of Astronomy and Astrophysics, Academia Sinica. 11F of Astronomy-Mathematics Building, AS/NTU No. 1, Section 4, Roosevelt Rd, Taipei 10617, Taiwan*
[33]*Department of Earth Sciences, National Taiwan Normal University, 88 Section 4, Ting-Chou Road, Taipei 11677, Taiwan*
[34]*Department of Earth Science Education, Seoul National University (SNU), 1 Gwanak-ro, Gwanak-gu, Seoul 08826, Republic of Korea*
[35]*Max-Planck-Institut für Extraterrestrische Physik, Giessenbachstrasse 1, D-85741 Garching bei München, Germany*
[36]*Department of Physics and Astronomy, University of Calgary, 2500 University Drive NW, Calgary, AB T2N 1N4, Canada*
[37]*Department of Astronomy, Faculty of Mathematics and Natural Sciences, Institut Teknologi Bandung, Jl. Ganesha 10, Bandung 40132 Indonesia*
[38]*Institute of Astronomy, National Central University, Jhongli 32001, Taiwan*
[39]*Physical Research Laboratory, Navrangpura, Ahmedabad 380009, Gujarat, India*
[40]*SOFIA Science Center, Universities Space Research Association, NASA, Ames Research Center, Moffett Field, CA 94035, USA*
[41]*Xinjiang Astronomical Observatory, Chinese Academy of Sciences, 830011 Urumqi, China*
[42]*IAPS-INAF, via Fosso del Cavaliere 100, I-00133 Rome, Italy*
[43]*Department of Physics and Astronomy, The Open University, Walton Hall, Milton Keynes MK7 6AA, UK*
[44]*Max-Planck-Institut für Radioastronomie, Auf dem Hügel 69, D-53121 Bonn, Germany*
[45]*Department of Physics and Astronomy, McMaster University, 1280 Main St. W, Hamilton, ON L8S 4M1, Canada*
[46]*Astrophysics Group, School of Physics, University of Exeter, Stocker Road, Exeter EX4 4QL, UK*
[47]*Department of Astronomy and Space Science, Chungnam National University, 99 Daehak-ro, Yuseong-gu, Daejeon 34134, Republic of Korea*
[48]*Jodrell Bank Centre for Astrophysics, School of Physics and Astronomy, University of Manchester, Oxford Road, Manchester M13 9PL, UK*
[49]*School of Physics and Astronomy, University of Leeds, Leeds LS2 9JT, UK*
[50]*National Astronomical Observatory of Japan, 2-21-1, Osawa, Mitaka, Tokyo 181-8588, Japan*
[51]*Department of Physics and Astronomy, Seoul National University, Seoul 151-747, Republic of Korea*
[52]*Graduate School of Pure and Applied Sciences, University of Tsukuba, 1-1-1 Tennodai, Tsukuba, Ibaraki 305-8571, Japan*
[53]*Tomonaga Center for the History of the Universe, University of Tsukuba, 1-1-1 Tennodai, Tsukuba, Ibaraki 305-8571, Japan*
[54]*Department of Physics and Atmospheric Science, Dalhousie University, Halifax, NS B3H 4R2, Canada*
[55]*College of Material Science and Chemical Engineering, Hainan University, Hainan 570228, China*
[56]*Key Laboratory of Modern Astronomy and Astrophysics, Nanjing University, Ministry of Education, Nanjing 210093, China*
[57]*Instituto de Radioastronomía y Astrofísica, Universidad Nacional Autonóma de México, Antigua Carretera a Pátzcuaro # 8701 Ex-Hda., San José de la Huerta, Morelia, Michoacán, C.P. 58089, México*
[58]*Radio Telescope Data Center, Center for Astrophysics, Harvard & Smithsonian, 60 Garden Street, Cambridge, MA 02138, USA*
[59]*Department of Astronomy, Peking University, 100871 Beijing, China*
[60]*Department of Astronomy, Yunnan University, Key Laboratory of Astroparticle Physics of Yunnan Province, Kunming 650091, China*

This paper has been typeset from a TEX/LATEX file prepared by the author.